

# On rising magnetic flux tube and formation of sunspots in a deep domain

H. Hotta <sup>1</sup>★ and H. Iijima <sup>2</sup>★

<sup>1</sup>*Department of Physics, Graduate School of Science, Chiba University, 1-33 Yayoi-cho, Inage-ku, Chiba 263-8522, Japan*

<sup>2</sup>*Division for Integrated Studies, Institute for Space-Earth Environmental Research, Nagoya University, Furocho, Chikusa-ku, Nagoya, Aichi 464-8601, Japan*

Accepted 2020 March 20. Received 2020 March 20; in original form 2020 February 9

## ABSTRACT

We investigate the rising flux tube and the formation of sunspots in an unprecedentedly deep computational domain that covers the whole convection zone with a radiative magnetohydrodynamics simulation. Previous calculations had shallow computational boxes ( $<30$  Mm) and convection zones at a depth of 200 Mm. By using our new numerical code Radition and RSST for Deep Dynamics (R2D2), we succeed in covering the whole convection zone and reproduce the formation of the sunspot from a simple horizontal flux tube because of the turbulent thermal convection. The main findings are as follows. (1) The rising speed of the flux tube is larger than the upward convection velocity because of the low density caused by the magnetic pressure and the suppression of the mixing. (2) The rising speed of the flux tube exceeds  $250 \text{ m s}^{-1}$  at a depth of 18 Mm, while we do not see any clear evidence of the divergent flow 3 h before the emergence at the solar surface. (3) Initially, the root of the flux tube is filled with the downflows, and then the upflow fills the centre of the flux tube during the formation of the sunspot. (4) The essential mechanisms for the formation of the sunspot are the coherent inflow and the turbulent transport. (5) The low-temperature region is extended to a depth of at least 40 Mm in the matured sunspot, with the high-temperature region in the centre of the flux tube. Some of the findings indicate the importance of the deep computational domain for the flux emergence simulations.

**Key words:** Sun: interior – Sun: photosphere – sunspots.

## 1 INTRODUCTION

Sunspots are one of the most prominent phenomena at the solar surface. Sunspots have a strong magnetic field ( $>3000$  G), which causes suppression of the convective heat transport and resultant darkening (see the review by Borrero & Ichimoto 2011). The origin of sunspots is thought to be deep in the convection zone (Parker 1955). The magnetic flux tube generated by the dynamo action is thought to rise to the surface and form sunspots at the solar surface (Zwaan 1985).

To understand the rising of the flux tube and the formation of sunspots using numerical simulations, realistic physics processes such as radiation, ionization, and thermal convection need to be considered. All of these are fundamentally important, and several numerical simulations of the formation of sunspots have been carried out using these processes. The first numerical simulation for sunspot formation including all these processes was performed by Cheung et al. (2010) using a 7.5-Mm deep computational box. The magnetic flux torus is inserted from the bottom boundary kinematically with a certain velocity. They find that the primary

mechanism of the formation of sunspots is the turbulent correlation against the mean diverging motion in the central region.

Rempel & Cheung (2014) performed simulations of emerging magnetic flux with a 15-Mm deep calculation domain. They find that the continuous upflow at the bottom boundary prevents the formation of sunspots at the photosphere; thus, they needed to change the boundary condition from the forced upflow to free open during the formation process. Later, Birch et al. (2016) compare their helioseismic observations of the surface divergent flow with Rempel & Cheung's (2014) calculations with different inserted velocities. Their observations do not find any clear evidence of the divergent flow at 3 h before the emergence time. In the simulations, the divergence flow 3 h before the emergence time is seen when the inserted velocity is large at the bottom boundary at a depth of 18 Mm. They conclude that the rising velocity should not be larger than  $150 \text{ m s}^{-1}$  at the bottom boundary to not having clear evidence of the divergent flow against the fluctuation caused by supergranulation.

Stein & Nordlund (2012) performed a sunspot simulation with a 20-Mm box in the vertical direction. The initial magnetic condition is the homogeneous flux sheet, and the turbulent convection spontaneously generates the flux rope and a resulting sunspot pair at the solar surface.

In these simulations, they need to assume the initial condition of the magnetic flux tube or sheet. To exclude this voluntariness,

\* E-mail: [hotta@chiba-u.jp](mailto:hotta@chiba-u.jp) (HH); [h.ijima@isee.nagoya-u.ac.jp](mailto:h.ijima@isee.nagoya-u.ac.jp) (HI)

Chen, Rempel & Fan (2017) adopt the bottom boundary condition referred from dynamo calculation (Fan & Fang 2014). There have been a number of dynamo calculations in which the large-scale magnetic field and cycle are reproduced (Ghizaru, Charbonneau & Smolarkiewicz 2010; Käpylä, Mantere & Brand enburg 2012; Nelson et al. 2013; Hotta, Rempel & Yokoyama 2016). None of these studies include the photosphere, and the typical top boundary is 30 Mm below the photosphere. Fan & Fang (2014) find spontaneous flux rising in their simulation, but the rising scale is about 800 Mm, which is much larger than what is expected from the photospheric observation. Thus, Chen et al. (2017) rescale the results from the dynamo calculation by a factor of 4–8 in space to fit their photospheric calculation. The time-scale and rising speed are also changed from the original dynamo calculation. In addition, the boundary condition is not influenced by what is occurring in the photospheric calculation. They find deep-seated downflow at the bottom boundary with the monolithic structure of the generated sunspot. They find that the converging flow accompanying the downflow collects the magnetic flux.

While the understanding of the formation of sunspots has been significantly improved in the last decade because of the realistic simulations presented, the computational domains of these studies are relatively shallow (<30 Mm) compared with the depth of the convection zone (200 Mm). We would expect some boundary effects on the resulting evolution of the flux tube and sunspots. To minimize the boundary influence to the evolution of the flux tube and a generated sunspot, we need to extend the calculation box. Recently, our new numerical code Radition and RSST for Deep Dynamics (R2D2, where RSST is the reduced speed of sound technique) succeeds in covering the whole convection zone in a calculation (Hotta, Iijima & Kusano 2019). In this study, we carry out a calculation of the rising flux tube with an unprecedentedly deep calculation box that covers the whole convection zone. Recently, Toriumi & Hotta (2019) perform a flux emergence simulation with a 140-Mm deep calculation box using the R2D2 code. In that study, we find spontaneous formation of the delta-type sunspot, which tends to have solar flares. In this study, we investigate the detailed mechanism of the rising of the flux tube and the formation of the sunspot in a deep domain in which the influence of the bottom boundary is expected to be small.

The rest of the paper is structured as follows. Section 2 describes the scheme and the setting of the numerical simulation. Section 3 shows the calculation results of the rising flux tube, formation process, and structure of the matured sunspot. In Section 4, we summarize our results and discuss the differences from previous studies. Future perspectives of flux emergence simulations are also discussed.

## 2 MODEL

### 2.1 Equations

We solve the three-dimensional magnetohydrodynamic (MHD) equations in the Cartesian geometry ( $x$ ,  $y$ ,  $z$ ) with the radiation transfer, where the  $z$ -direction is vertical and the  $x$ - and  $y$ -directions are horizontal. In this study,  $z = 0$  is the solar surface, which is  $R_{\odot} = 696$  Mm from the centre of the sun. The equations are solved with the R2D2 code. The MHD equations are expressed as

$$\frac{\partial \rho_1}{\partial t} = -\frac{1}{\xi^2} \nabla \cdot (\rho \mathbf{v}), \quad (1)$$

$$\frac{\partial}{\partial t} (\rho \mathbf{v}) = -\nabla \cdot (\rho \mathbf{v} \mathbf{v}) - \nabla p_1 - \rho_1 g \mathbf{e}_z + \frac{1}{4\pi} (\nabla \times \mathbf{B}) \times \mathbf{B}, \quad (2)$$

$$\frac{\partial \mathbf{B}}{\partial t} = \nabla \times (\mathbf{v} \times \mathbf{B}), \quad (3)$$

$$\rho T \frac{\partial s_1}{\partial t} = \rho T (\mathbf{v} \cdot \nabla) s + Q, \quad (4)$$

$$p_1 = p_1(\rho, s), \quad (5)$$

where  $\rho$ ,  $\mathbf{v}$ ,  $\mathbf{B}$ ,  $p$ ,  $T$ ,  $s$ ,  $g$ , and  $Q$  are the density, fluid velocity, magnetic field, gas pressure, temperature, entropy, gravitational acceleration, and radiative heating, respectively. The subscript 1 indicates the perturbation from the stationary one-dimensional stratification indicated with subscript 0. Thus, the thermodynamic variables are expressed as

$$\rho = \rho_0 + \rho_1, \quad (6)$$

$$p = p_0 + p_1, \quad (7)$$

$$s = s_0 + s_1. \quad (8)$$

In this study, we do not assume that the perturbation is smaller than the stationary background stratification, i.e.  $\rho_1 < \rho_0$  is not assumed. The background stratification is calculated with the hydrostatic equation with the help of the Model S (Christensen-Dalsgaard et al. 1996). See Appendix A for the details of the calculation procedure.

The equations are solved with the fourth-order spatial derivative (see Appendix B for details) and the four-step Runge–Kutta method for the time integration (Vögler et al. 2005). To maintain the stability of the calculation, we adopt the slope-limited diffusion suggested by Rempel (2014).

We use the equation of state considering the partial ionization effect with the OPAL repository (Rogers, Swenson & Iglesias 1996). We switch the linear and table equations of state to address the significant change of the perturbation through the convection zone. We evaluate the value

$$c_{\text{eos}} = \max \left( \frac{|s_1|}{s_0}, \frac{|\rho_1|}{\rho_0} \right). \quad (9)$$

If  $c_{\text{eos}}$  exceeds  $10^{-2}$ , we use the table equation of state; otherwise, the linear equation of state

$$p_1 = \left( \frac{\partial p}{\partial \rho} \right)_s \rho_1 + \left( \frac{\partial p}{\partial s} \right)_\rho s_1, \quad (10)$$

is used.  $(\partial p / \partial \rho)_s$  and  $(\partial p / \partial s)_\rho$  are prepared with the background stratification and only depend on the height ( $z$ ). Regarding the table equation of state, we prepare a  $64 \times 64$  grid on the density and entropy.

We adopt the RSST (Hotta et al. 2012; Hotta, Rempel & Yokoyama 2015; Iijima, Hotta & Imada 2019) for the equation of continuity to deal with the low Mach number flow in the deep convection zone. By using the RSST, we try to keep the Mach number throughout the convection zone. To this end, we set the RSST factor,

$$\xi(z) = \max \left( 1, \xi_0 \left[ \frac{\rho_0(z)}{\rho_b} \right]^{1/3} \frac{c_s(z)}{c_b} \right). \quad (11)$$

Here, we adopt  $\xi_0 = 160$ .  $\rho_b = 0.2 \text{ g cm}^{-3}$  and  $c_b = 2.2 \times 10^7 \text{ cm s}^{-1}$  are the density and the speed of sound around the base of the convection zone, respectively.  $c_s = \sqrt{(\partial p / \partial \rho)_s}$  is the local adiabatic speed of sound. When the energy flux is fixed, the convection

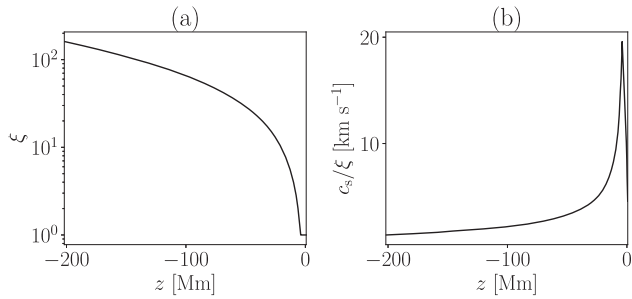


**Figure 1.** (Panel a) The RSST factor  $\xi$  and (panel b) the reduced speed of sound  $c_s/\xi$  are shown.

velocity scales with  $\rho_0^{-1/3}$  in the mixing length theory. This setting approximately maintains the Mach number. Fig. 1 shows the RSST factor  $\xi$  (panel a) and the reduced speed of sound  $c_s/\xi$  (panel b). Hotta et al. (2012) show that if the Mach number estimated with the reduced speed of sound is smaller than 0.7, the RSST cause no side effect on the result.

We limit the Alfvén velocity to  $40 \text{ km s}^{-1}$  to deal with the low- $\beta$  region above the photosphere (Rempel, Schüssler & Knölker, 2009b). This does not affect what is occurring at the photosphere.

The radiative heating  $Q$  is calculated with the radiative transfer equation; the details are shown in Appendix C.

We calculate the thermal convection with the top boundary at  $z = -7 \text{ Mm}$  for 90 d. The thermal convection around the photosphere is very fast, and we exclude this layer for accelerating the calculation. Then, we include the photosphere with the top boundary at 700 km above the photosphere and continue the calculation for 5 d. This procedure is justified because the existence of the photosphere does not change the deep structure (Hotta et al. 2019).

The calculation domain extends 98.304 Mm horizontally for  $x$ - and  $y$ -directions. The vertical calculation extent is from the base of the convection zone,  $z = -0.29 R_\odot$ , to  $z = 700 \text{ km}$ . The number of grid points in each horizontal direction is 1024, and the grid spacing is 96 km, and this is acceptable to resolve the photosphere. In the vertical direction, we use 512 grid points and non-uniform grid spacing, and this is 48 km around the photosphere and 900 km around the base of the convection zone.

## 2.2 Initial condition

We adopt the Lundquist solution (Lundquist 1950) for the linear force-free flux tube as follows:

$$B_x(r) = B_{\text{tb}} J_0(\alpha r), \quad (12)$$

$$B_z(y, z) = B_\theta(r) \frac{y - y_{\text{tb}}}{r}, \quad (13)$$

$$B_y(y, z) = -B_\theta(r) \frac{z - z_{\text{tb}}}{r}, \quad (14)$$

$$B_\theta(r) = B_{\text{tb}} J_1(\alpha r), \quad (15)$$

$$r = \sqrt{(y - y_{\text{tb}})^2 + (z - z_{\text{tb}})^2}, \quad (16)$$

$$\alpha = \frac{a_0}{r_{\text{tb}}}, \quad (17)$$

where  $a_0 = 2.404825$  is the first root of  $J_0$ , and  $r_{\text{tb}} = 9.9 \text{ Mm}$  is the radius of the flux tube.  $J_0$  and  $J_1$  are the Bessel functions. Here, we adopt  $z_{\text{tb}} = -0.05 R_\odot$ , i.e. the initial magnetic flux tube

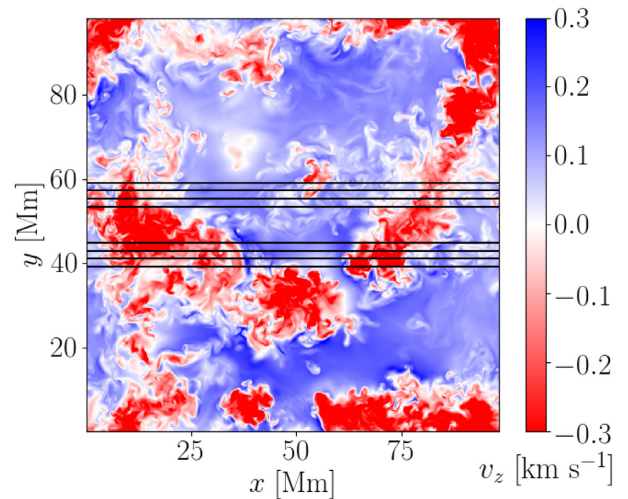


**Figure 2.** Initial setup of the magnetic flux tube at  $z = -35 \text{ Mm}$ . The colour contour shows the vertical velocity  $v_z$ , and the contour lines show the axial magnetic field  $B_x$ . Each contour line shows 0, 2.5, 5, and 7.5 kG.

is located about 35 Mm below the photosphere and  $B_{\text{tb}} = 10^4 \text{ G}$  for the magnetic field strength at the centre of the flux tube. This leads to a total flux of  $1 \times 10^{22} \text{ Mx}$ .  $y_{\text{tb}}$  is an arbitrary parameter with which the horizontal location of the flux tube is determined. With our choice, the initial flux tube is located in the centre of the computational domain. Fig. 2 shows the initial flux tube condition at  $z = -0.05 R_\odot$ . The initial flux tube is caught by the two coherent downflows. Note that the left downflow is larger and more coherent. Because the initial magnetic flux tube is force-free, we do not change any thermodynamic variable, i.e. the density, pressure, or entropy from the prepared hydrodynamic calculation. Thus, the magnetic flux initially does not have any buoyancy by the magnetic field, but the inertia of the convective flow can distort the magnetic flux tube.

## 3 RESULTS

### 3.1 Magnetic flux and area

Fig. 3 shows the temporal evolution of unsigned magnetic flux on  $\tau = 1$  surface (panel a) and the area of the sunspot (panel b). In Fig. 3(a), the black line shows the unsigned magnetic flux integrated over all horizontal domains. The red and blue lines show the unsigned magnetic flux with the emergent intensity less than 80 and 50 per cent of the averaged quiet sun intensity  $I_\odot$ , respectively. Fig. 3(b) shows the area with the emergent intensity less than  $0.8 I_\odot$  (red) and  $0.5 I_\odot$  (blue). For making Fig. 3(b), we use the Gaussian filter with a width of 1 Mm. The unsigned magnetic flux reaches its maximum of  $2.7 \times 10^{22} \text{ Mx}$  at  $t = 63.7 \text{ h}$ . We follow the definition of the emergence time suggested by Leka et al. (2013), in which the unsigned magnetic flux reaches 10 per cent of the maximum magnetic flux. The emergence time in this calculation is  $t = 37 \text{ h}$ . After the magnetic flux reaches its maximum, the magnetic flux begins to decrease. Around  $t = 175 \text{ h}$ , almost all the magnetic flux in the sunspot  $I < 0.5 I_\odot$  disappears, leading to approximate emergence and decay rates ( $d\Phi/dt$ ) of  $9 \times 10^{20}$  and  $-2 \times 10^{20} \text{ Mx h}^{-1}$ , respectively. These values are similar to those in Rempel & Cheung (2014). We note that they determine the rising speed of the flux tube at the bottom boundary, while the

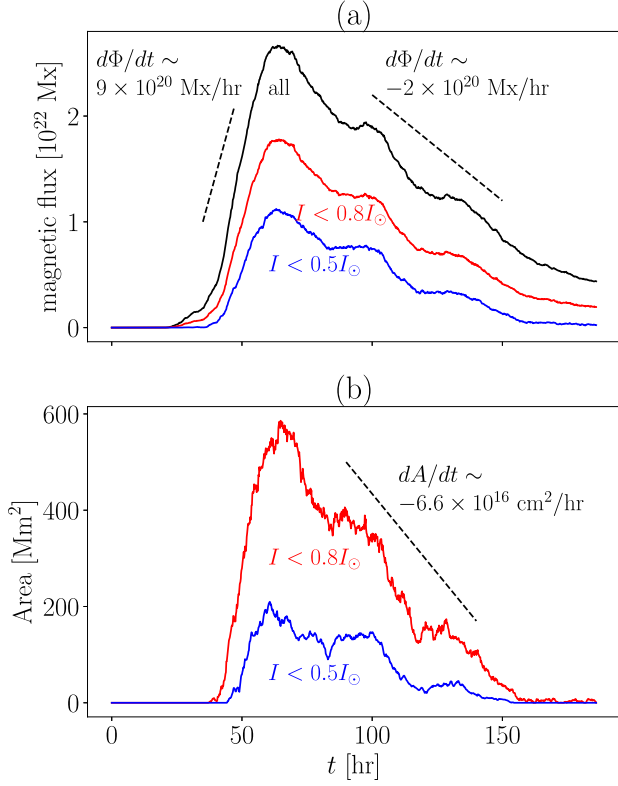


**Figure 3.** Temporal evolution of the unsigned magnetic flux (panel a) and sunspot area (panel b) at the  $\tau = 1$  surface is shown. (Panel a) The black line shows the unsigned magnetic flux of all areas. The red and blue lines show the unsigned magnetic flux at the area with  $I < 0.8I_{\odot}$  and  $I < 0.5I_{\odot}$ , respectively, where  $I$  and  $I_{\odot}$  are the emergent intensity and that in the quiet region, respectively. (Panel b) The area of corresponding intensity is shown. The format of the lines is the same as in panel a.

combination of the convection and the magnetic field determines the rising property in this calculation.

Compared with the observations, Otsuji et al. (2011) and Norton et al. (2017) show the relation of the maximum sunspot flux  $\Phi_{\max}$  and the emergence rate  $(d\Phi/dt)_e$  as  $(d\Phi/dt)_e = 9.6 \times 10^7 \Phi_{\max}^{0.57}$  and  $7.8 \times 10^{11} \Phi_{\max}^{0.36}$ , where both are in the unit of  $\text{Mx h}^{-1}$ . The maximum flux of the current simulation  $\Phi_{\max} = 2.7 \times 10^{22}$  Mx leads to  $(d\Phi/dt)_e = 6 \times 10^{20}$  Mx and  $9 \times 10^{19}$  by using Otsuji et al.'s (2011) and Norton et al.'s (2017) relations, respectively. In addition, Namekata et al. (2019) show that the 95 per cent confidence interval of the emergence rate reaches  $(d\Phi/dt)_e = 7 \times 10^{20}$   $\text{Mx h}^{-1}$  with  $\Phi_{\max} = 2.7 \times 10^{22}$  Mx. Compared with these observational results, this numerical simulation shows a slightly larger emergence rate.

Regarding the decay rate of the sunspot, Hathaway & Choudhary (2008) show the observational relation between the sunspot area  $A$  and the dissipation rate  $dA/dt$  as  $dA/dt = -3 \times 10^{16} - 5 \times 10^{-3}A$  [ $\text{cm}^2 \text{h}^{-1}$ ]. We assume that the mean magnetic field strength is 2000 G, which is used in Namekata et al. (2019). This relation leads to  $d\Phi/dt = -1.9 \times 10^{20}$   $\text{Mx h}^{-1}$ , which is consistent with the simulation in this study. Fig. 3(b) shows that the area of the sunspot reaches its maximum  $A = 5.9 \times 10^{18}$   $\text{cm}^2$  at  $t = 65$  h and that the area decreases to zero at  $t = 154$  h. This leads to the decay rate of  $dA/dt = -6.6 \times 10^{16}$   $\text{cm}^2 \text{h}^{-1}$ . The Hathaway & Choudhary (2008) relation leads to  $dA/dt = -6.0 \times 10^{16}$   $\text{cm}^2 \text{h}^{-1}$  for our case. Also, in terms of area, the calculation result is consistent with the observation.

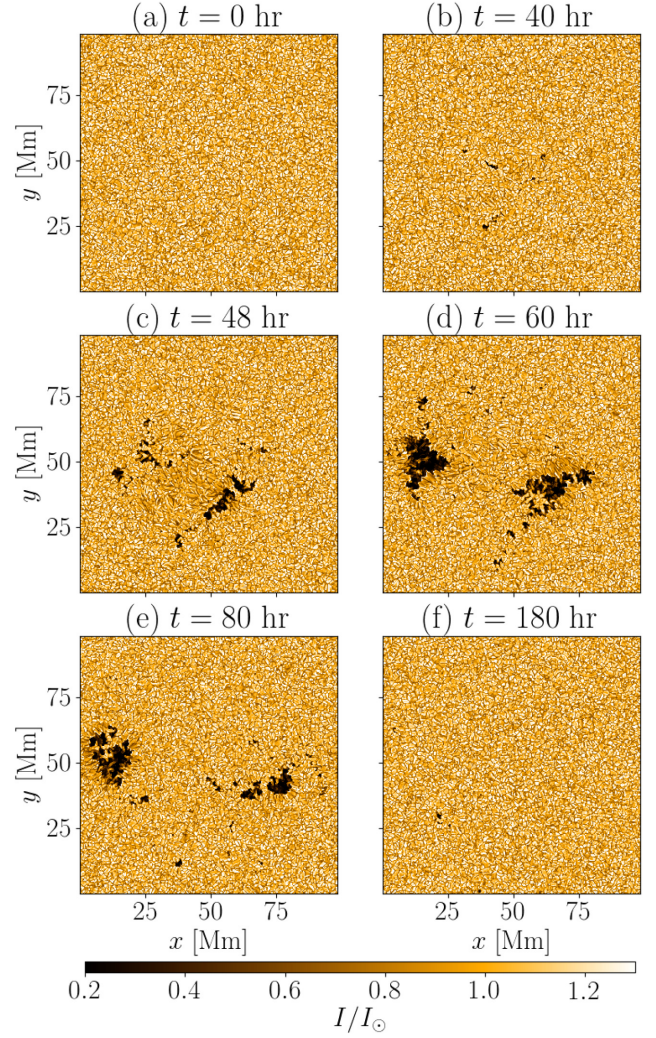


**Figure 4.** The temporal evolution of the emergent intensity is shown. The intensity is normalized with the mean quiet sun intensity  $I_{\odot}$ .

### 3.2 Overall evolution

Figs 4 and 5 show the emergent intensity and line-of-sight magnetic field  $B_z$  at  $\tau = 1$  surface, respectively. Around the emergence time  $t = 37$  h, we begin to see small pores in the intensity map (Fig. 4b) and a diffused pattern in the magnetic field map (Fig. 5b). As time progresses, the small pores merge and construct the large-scale structure. At  $t = 48$  h, we observe elongated granules between the positive and negative spots (Figs 4c and 5c). When the photospheric magnetic flux reaches its maximum, a coherent sunspot appears (Figs 4d and 5d). While we see some evidence of the penumbra around the sunspot, the reproduced penumbra is much less prominent than the observation. Rempel (2012) shows that the existence of the penumbra is significantly affected by the top boundary condition. Here, we use the potential magnetic field condition, while Rempel (2012) argues that the horizontally inclined magnetic field at the top boundary is required for a prominent penumbra. We also note that Rempel et al. (2009a) show that the penumbra can be observed between two sunspots because the horizontal magnetic field is expected between them. In this study, the matured sunspots are far apart from each other, and even the penumbra between the sunspot pair cannot be observed.

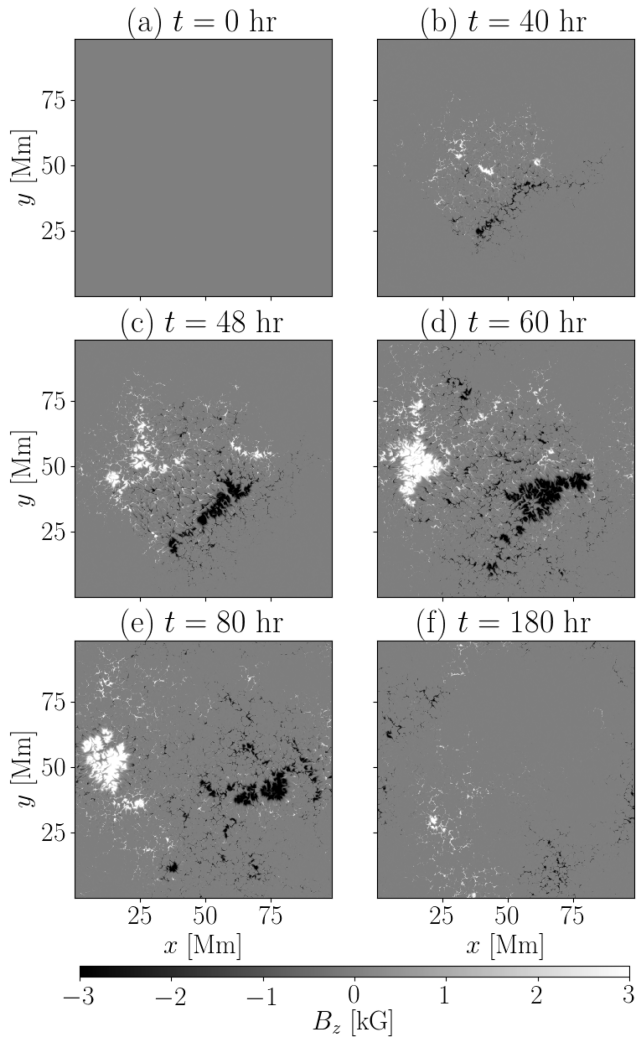


**Figure 5.** The temporal evolution of the line-of-sight magnetic field ( $B_z$ ) at the  $\tau = 1$  surface is shown.

After the magnetic flux reaches its maximum, the sunspots begin to lose their magnetic flux. At  $t = 80$  h, the right sunspot loses significant flux, while the left sunspot keeps a coherent shape with some bright features in the umbra (Fig. 5e). At  $t = 180$  h, almost all the magnetic flux disappears from the umbra (Figs 4f and 5f).

Fig. 6 shows the three-dimensional structure of the magnetic field deep in the convection zone. At  $t = 20$  h, the magnetic field shows an  $\Omega$ -shape structure with two anchoring downflows and a broad upflow in the centre region (Fig. 6b). At  $t = 40$  h (Fig. 6c), which is around the emergence time, a significant fraction of the magnetic flux reaches the near-surface layer ( $z > -10$  Mm). At  $t = 60$  h (Fig. 6d), which is around the time of the maximum photospheric magnetic flux, the root of the left sunspot reaches a depth of around 80 Mm, while the root of the right sunspot remains at a depth of around 30 Mm. Below the photosphere, the magnetic field of the sunspot is mostly vertical. At  $t = 80$  h (Fig. 6e), the sunspots begin to decay; at the same time, the subsurface structure is destroyed. At  $t = 180$  h (Fig. 6f), when the sunspot disappears almost completely, most of the flux is transported downward, and coherent features can still be seen in the deep region below a depth of 60 Mm.

The Coriolis force is an important factor for the tilt angle (Wang & Sheeley 1991) and the asymmetry of the sunspot pair (D’Silva &

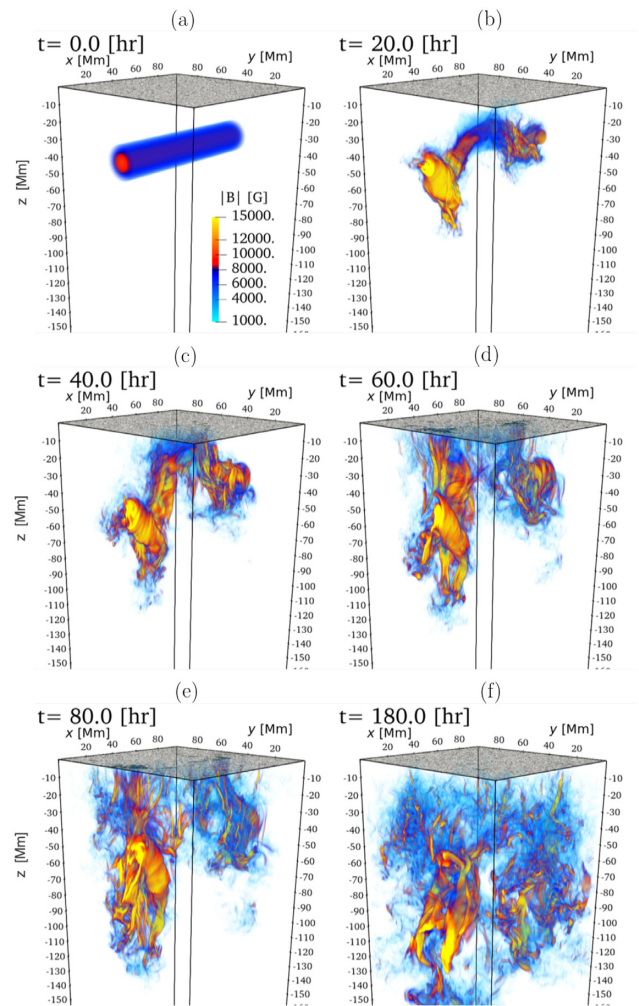


**Figure 6.** Temporal evolution of the three-dimensional structure of the overall magnetic field is shown. The volume rendering shows the magnetic field strength, and the grey surface around the top of the computational domain shows the emergent intensity.

Choudhuri 1993). Cheung et al. (2010) show an almost symmetric sunspot pair because of their almost symmetric initial condition and setting. Rempel & Cheung (2014) show an asymmetric sunspot pair resulting from the horizontal flow mimicking the Coriolis force-induced flow. Chen et al. (2017) also show asymmetry resulting from the boundary condition motivated by the dynamo calculation influenced by the Coriolis force. While the Coriolis force must be important to generate a statistical trend of the sunspot pair feature (Weber, Fan & Miesch 2011), our calculation without the Coriolis force can also cause some asymmetry in the sunspot pair. The asymmetry in this study reflects the convection flow structure in the deep convection zone. The initial condition (Fig. 2) shows that the left downflow has a more circular shape than does the right downflow, which shows an elongated feature. Interestingly, the emerging sunspot follows this morphology. Fig. 7 shows the flow and magnetic structure in deep layers at  $t = 60$  h. Color and line contours show the vertical velocity ( $v_z$ ) and magnetic field ( $B_z$ ), respectively. At a depth of at least 30 Mm (Fig. 7b), we can still observe the asymmetry of the magnetic feature, i.e. the positive magnetic feature (solid line) shows the circular shape, while the negative feature (dashed line) is elongated. In the deeper layer, the

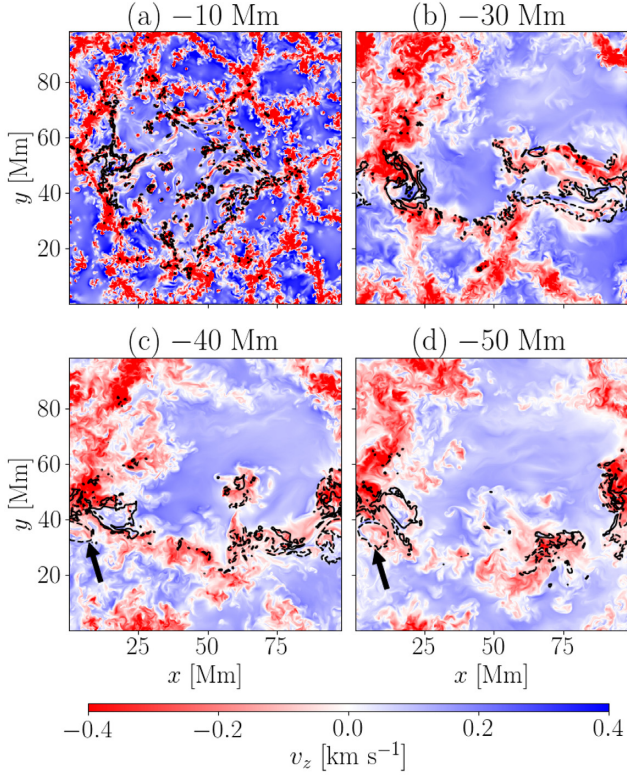


**Figure 7.** The flow and magnetic structure in the deep layer at  $t = 60$  h is shown. Panels a, b, c, and d show the layers at  $z = -10, -30, -40,$  and  $-50$  Mm, respectively. The colour contour shows the vertical velocity ( $v_z$ ), and the black contour lines show the vertical magnetic field ( $B_z$ ) of 5000 G (solid) and  $-5000$  G (dashed).

positive feature maintains a circular shape. The negative feature crosses the boundary and reaches the other side indicated with a black arrow in Fig. 7(c) because of the periodic boundary condition. At a depth of 50 Mm, the negative feature has a circular shape (black arrow in Fig. 7d). We note that the time-scale of the convection at 50 Mm depth is about 5 d, and the structure of the magnetic flux tube has not been distorted well at this depth. This result indicates that the shape of the sunspot is influenced by the deep convection structure at least 30 Mm below the photosphere.

### 3.3 Rising mechanism of flux tube

In this section, we investigate the rising process of the flux tube mainly around the centre region ( $x = 41$  Mm). Fig. 8 shows the temporal evolution of the rising flux tube. The left- and right-hand panels show the vertical velocity  $v_z$  and Alfvén velocity of the axial field  $c_A = B_x / \sqrt{4\pi\rho}$ , respectively. To investigate the motion of the flux tube, we adopt the following definition of the centre of the flux tube. Basically, we use a clumping method. We detect clumps of the region having an Alfvén velocity beyond a given threshold. With iteration, we survey the threshold  $c_{A0}$  with which the largest clump has a magnetic flux of  $6 \times 10^{21}$  Mx, where the magnetic flux is estimated with  $B_x$ . The largest clump ( $S_c$ ) in each time-step is defined as the rising flux tube. The centre of the flux tube ( $y_c, z_c$ ) is defined as follows:

$$y_c = \frac{\int_{S_c} y c_A dS}{\int_{S_c} c_A dS}, \quad (18)$$

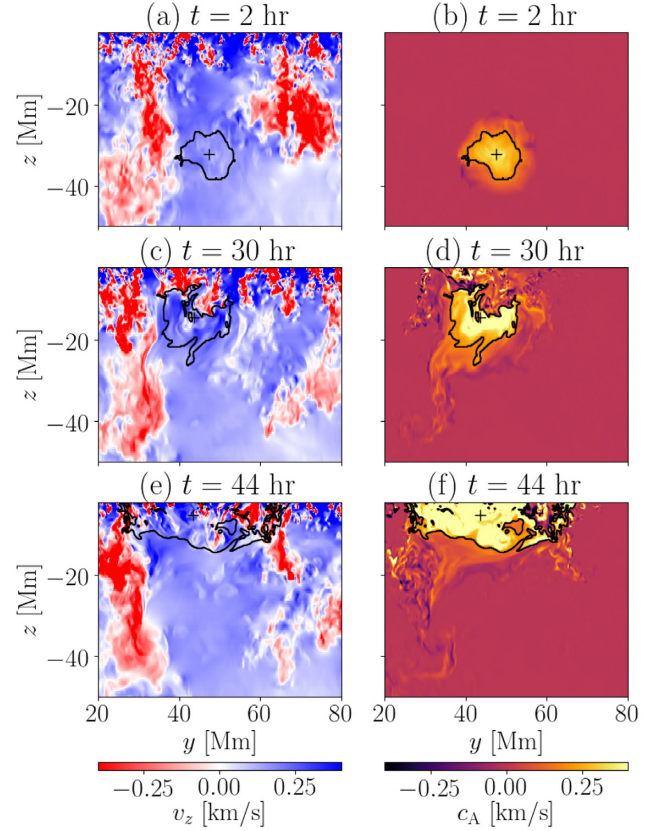


**Figure 8.** Rising process at  $x = 41$  Mm. The left- and right-hand panels show the vertical velocity  $v_z$  and Alfvén velocity of the axial field  $c_A = B_x / \sqrt{4\pi\rho}$ , respectively. The top, middle, and bottom panels show results at  $t = 2, 30,$  and  $44$  h, respectively. The black lines show the boundary of the detected flux tube. The black cross shows the centre of the flux tube.

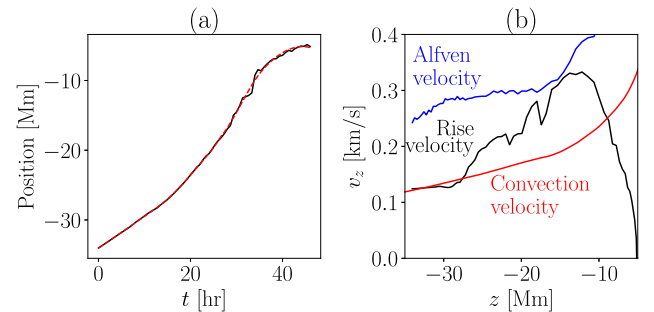


**Figure 9.** (Panel a) The time evolution of the centre of the flux tube in height  $z_c$  is shown. The black line is the raw data, and the red line is filtered data for estimating the rising velocity. (Panel b) The black line shows the rising speed of the centre of the flux tube. The red line shows the rms convection velocity in the calculation without the magnetic field. The blue line shows the local Alfvén velocity  $c_A$  averaged in the flux tube ( $S_c$ ).

$$z_c = \frac{\int_{S_c} z c_A dS}{\int_{S_c} c_A dS}. \quad (19)$$

The boundary and centre of the flux tube are shown with black lines and black crosses in Fig. 8, respectively. The time evolution of the centre of the flux tube is shown in Fig. 9. Fig. 9(a) shows the vertical position of the centre of flux tube  $z_c$ . In the beginning, the rising speed increases with time, when the flux tube reaches the

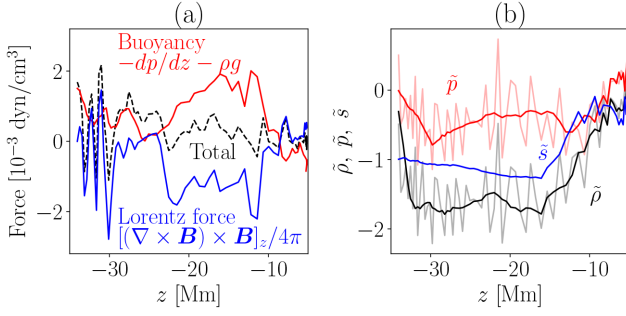


**Figure 10.** (Panel a) The mean forces in the flux tube are shown. The red and blue lines show the buoyancy and Lorentz force, respectively. The black line shows the total force, including the inertia. (Panel b) The mean normalized density, pressure, and entropy in the flux tube are shown. The light colour in panel (b) shows the values before filtering out the sound waves.

solar surface, the speed is reduced. The time profile of the vertical position is not smooth because of sudden merging and splitting. To evaluate the rising speed, we use a Savitzky–Golay filter for the vertical position, which is shown as the red line in Fig. 9(a). By using the filtered profile of the vertical position, we estimate the rising speed of the centre of the flux tube. The black line in Fig. 9(b) shows the rising speed of the flux tube. The red line shows the root-mean-square (rms) upflow convection velocity in a hydrodynamic run, i.e. without the magnetic field. We note that the downflow convection velocity is typically larger than the upflow velocity. The blue line shows the mean Alfvén velocity in the flux tube. In the beginning, the rising speed is almost the same as the upward convection velocity. This is natural because the initial flux tube is force-free and the flux tube needs to obey the convective flow. As time progresses, the rising speed exceeds the convection velocity, indicating some contribution of the magnetic field to the rising process. Even at the end of the rising process, the rising speed does not reach the local Alfvén velocity. This result indicates that the rising process is neither a pure magnetic nor a pure convective process.

To understand the rising mechanism, we investigate the vertical equation of motion. Fig. 10(a) shows the vertical forces averaged in the flux tube. Before evaluating the equation of motion, we filtered out the sound waves in the phase space (Georgobiani et al. 2007). The equation of motion in the vertical direction is

$$\rho \frac{\partial v_z}{\partial t} = -\rho (\mathbf{v} \cdot \nabla) v_z - \frac{\partial p}{\partial z} - \rho g + \frac{1}{4\pi} [(\nabla \times \mathbf{B}) \times \mathbf{B}]_z. \quad (20)$$

The red and blue lines in Fig. 10(a) show the buoyancy ( $-dp/dz - \rho g$ ) and Lorentz force ( $[(\nabla \times \mathbf{B}) \times \mathbf{B}]_z/4\pi$ ), respectively. The moving flux tube can be roughly regarded as a Lagrangean parcel in the  $y$ - $z$  plane. Only the contribution from the inertia term ( $-\rho (\mathbf{v} \cdot \nabla) v_z$ ) to the motion of the rising flux tube is ( $-\rho v_x dv_x/dx$ ). The black line is the sum of these terms. The buoyancy and total force direct upward during the rising process, while the Lorentz force directs downward. The main contribution of the Lorentz force is magnetic tension. The roots of the magnetic flux are anchored in the deep layer; thus, the magnetic tension in the rising part directs downward. Fig. 10(b) shows the mean normalized density, pressure, and entropy in the flux tube. The normalization procedure, i.e. the tilde, for quantities is defined as follows:

$$\tilde{\rho} = \frac{\rho - \langle \rho \rangle_{\text{hd}}}{\rho_{\text{rms}}(\text{hd})}, \quad (21)$$

$$\tilde{p} = \frac{p - \langle p \rangle_{\text{hd}}}{\rho_{\text{rms}}(\text{hd})} \left( \frac{\partial \rho}{\partial p} \right)_s, \quad (22)$$

$$\tilde{s} = \frac{s - \langle s \rangle_{\text{hd}}}{\rho_{\text{rms}}(\text{hd})} \left( \frac{\partial \rho}{\partial s} \right)_p, \quad (23)$$

where  $\langle q \rangle_{\text{hd}}$  and  $q_{\text{rms}}(\text{hd})$  are the horizontal average and rms value of a quantity  $q$  in the calculation without the magnetic field, respectively. After normalization, the density, pressure, and entropy are related as  $\tilde{\rho} = \tilde{s} + \tilde{p}$ . We also note that because  $(\partial \rho / \partial s)_p$  is negative, the negative value of  $\tilde{s}$  corresponds to a positive perturbation of the entropy  $s_1 - \langle s_1 \rangle_{\text{hd}}$  and vice versa. The result shows that the mean normalized density in the flux tube is significantly low (the perturbation is 1.7 times larger than the rms value); this is the primary driver of the rising flux tube. There are two contributions to the low density in the flux tube. The first is the low pressure caused by the magnetic pressure. After the rising starts, the twist becomes relaxed and the force-free balance is destroyed. Then, the gas pressure gradient force plays a role in maintaining the flux tube and decreasing the gas pressure in the flux tube. Because the initial flux tube is force-free, the magnetic tension plays a role in balancing the magnetic pressure, even during the rising process; thus, the gas pressure is not significantly low in this case. The other contribution to the low density is the high entropy maintained by the suppression of the mixing. The initial magnetic flux tube is located in the upflow region and has higher entropy than does the surrounding plasma. As seen in Figs 8(c) and (d), the magnetic field suppresses the mixing between upflows and downflows. In an ordinary medium in the convection zone, the upflow warm medium is mixed in a mixing length and loses its high entropy, but this magnetic flux tube can avoid this process and maintain high entropy, leading to continuously low density in the flux tube and further acceleration. Fig. 10(b) shows that the high entropy is the main contribution to the low density in the flux tube.

### 3.4 Surface flow prior to emergence time

In this section, we investigate the divergent flow prior to emergence time to compare the results with Birch et al. (2016), in which clear divergent flow is not seen at 3 h before the flux emergence.

To this end, we follow a similar procedure to that of Birch et al. (2016). We take the divergence of the horizontal flow at  $\tau = 1$  surface and the Gaussian filter with a 6-Mm window. Fig. 11 shows the horizontal divergence  $\nabla_h \cdot \mathbf{v}$  at  $\tau = 1$  surface at  $t = 34$  and 37, and 42 h. The standard error of the distribution is  $3 \times 10^{-5} \text{ s}^{-1}$ , and the black line in Fig. 11 shows the  $3\sigma$  value. We again note that  $t = 37$  h is the emergence time. Panels (a) and (c) show the results 3 h before and 5 h after the emergence time. While we see a clear divergent flow at and after the emergence time (panels b and c), we do not see it 3 h before the emergence time (panel a). This result is consistent with the observation of Birch et al. (2016). In contrast, the rising speed of the flux tube exceeds  $250 \text{ m s}^{-1}$  at a depth of 18 Mm, while Birch et al. (2016) suggest that the rising speed is no larger than  $150 \text{ m s}^{-1}$  to avoid divergent flow prior to the emergence time.

Fig. 12 shows the temporal evolution of the horizontal divergence at  $\tau = 1$  surface. The black and red lines show the maximum and top 1 per cent value of the divergent flow, respectively. This also indicates that the clear evidence of the divergent flow is seen at only 1 h before the emergence time.

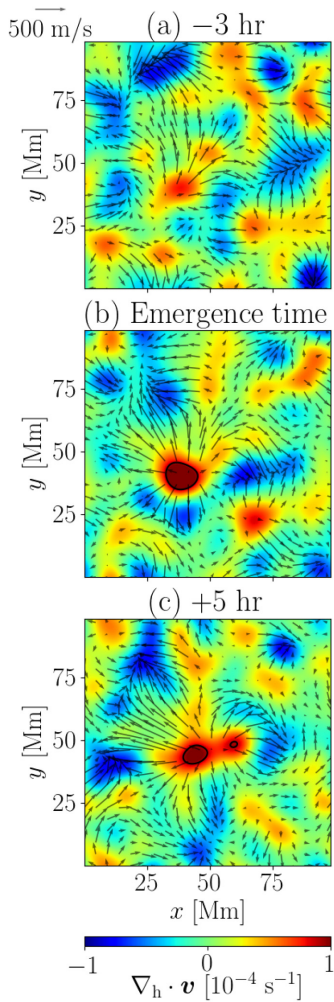


**Figure 11.** The divergence of the horizontal flow at  $\tau = 1$  surface. Panel (b) shows the result at the emergence time ( $t = 37$  h). Panels (a) and (c) show the results 3 h before and 5 h after the emergence time, respectively. The arrows show the horizontal flow. The black contour line shows the  $3\sigma$  value of the horizontal divergence ( $\nabla_{\text{h}} \cdot \mathbf{v} = 9 \times 10^{-9} \text{ s}^{-1}$ ).

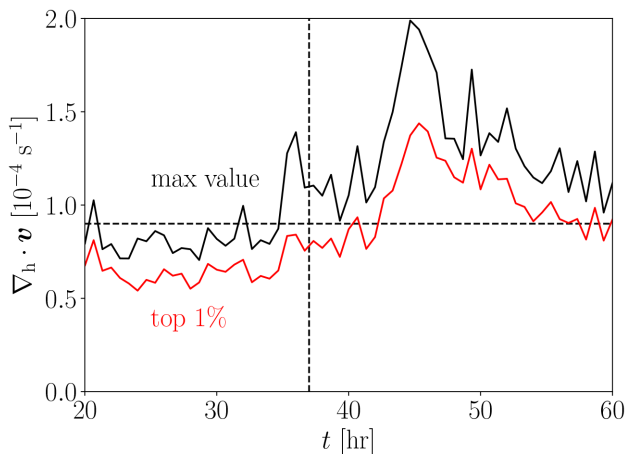


**Figure 12.** Temporal evolution of the horizontal divergence at  $\tau = 1$  surface. The black and red lines show the maximum and top 1 per cent value of the divergence, respectively. The horizontal and vertical dashed lines show the  $3\sigma$  value and emergence time, respectively.

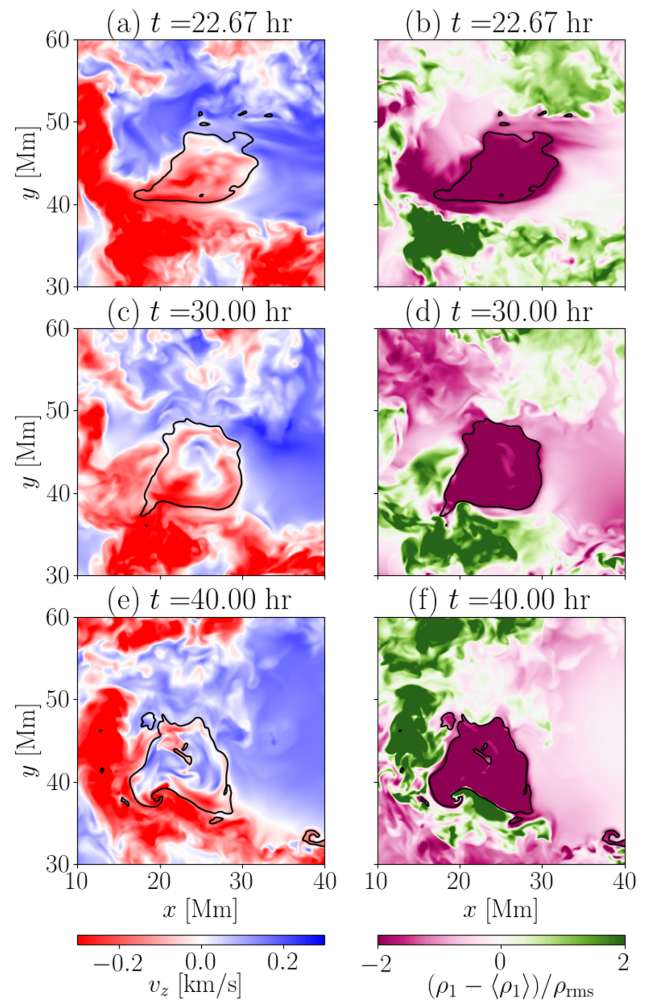


**Figure 13.** The left- and right-hand panels show the vertical flow and normalized density at  $z = -30$  Mm, respectively. The top, middle, and bottom panels show the results at  $t = 22.67, 30,$  and  $40$  h, respectively. The black contour lines show vertical magnetic field  $B_z$  of 7000 G, roughly indicating the magnetic flux tube.

### 3.5 Flow in flux tube

In this section, we investigate the flow in the flux tube during the flux emergence process. First, we discuss the vertical flow at  $z = -30$  Mm in detail. Then, we discuss the flow at different heights. Fig. 13 shows the temporal evolution of the vertical flow and the density in the flux tube. From this section, we focus on the left coherent positive sunspot. Because the root of the sunspot is created with the downflow from the horizontal magnetic flux tube, the root is initially filled with the downflow (Fig. 13a:  $t = 22.67$  h). This is somewhat consistent with Chen et al. (2017), in which the strong magnetic concentration occurs at a coherent downflow in the deep layer. A difference is seen in the following evolution. The flow in the flux tube changes signs around  $t = 30$  h in Fig. 13(c). After the sunspot is formed (Fig. 13e:  $t = 40$  h), the flux tube is filled with the upflow. During this process, the flux tube is filled with the low-density medium (Figs 13b, d, and f).

Here, we define the flux tube as the largest clump in which the vertical magnetic field exceeds the threshold value of 7000 G. Fig. 14(a) shows the temporal evolution of the mean vertical flow in the flux tube. In the beginning, the flux tube is filled with



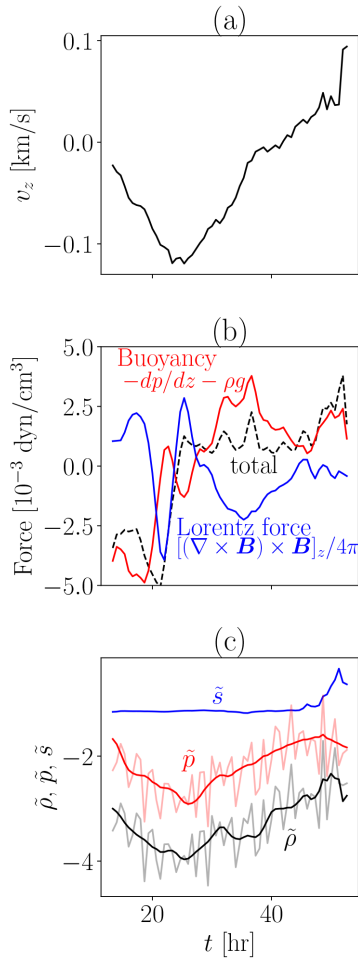


**Figure 14.** (Panel a) Temporal evolution of the mean vertical velocity in the flux tube at a depth of 30 Mm is shown. (Panel b) The force balance in the flux tube at a depth of 30 Mm is shown. The red, blue, and black lines show the buoyancy, Lorentz, and total forces, respectively. (Panel c) The black, red, and blue lines show the normalized density, pressure, and entropy, respectively. The light colour in panel (c) shows the value before filtering out the sound waves.

the downflow. Around  $t = 23$  h, the downflow stops increasing in amplitude. Around  $t = 40$  h, the vertical flow changes signs. Afterward, the amplitude of the upflow increases continuously. Fig. 14(b) shows the force balance in the flux tube. The red and blue lines show the buoyancy and the Lorentz force, respectively. The flux tube roughly acts as the Lagrangean parcel in the  $x$ - $y$  plane. Thus, for the total dynamics, the contribution from the inertia term is the vertical inertia term  $-\rho v_z \partial v_z / \partial z$ . The black line in Fig. 14(b) shows the sum of the buoyancy, Lorentz force, and vertical inertia terms. The total force is consistent with the temporal evolution of the vertical velocity in the flux tube. Around  $t = 23$  h, the total force changes its sign and keeps the positive value after that. The main driver of the upflow in the flux tube is the buoyancy. Fig. 14(c) shows the normalized density, pressure, and entropy averaged in the flux tube (see equations 21–23). In this case, the main contribution of the low density is the low gas pressure caused by the adiabatic expansion from the Lorentz force.

Fig. 15 shows the azimuthally averaged values in the polar coordinate. Because the generated sunspot and its flux tube are tangling along the vertical direction, different heights cannot share

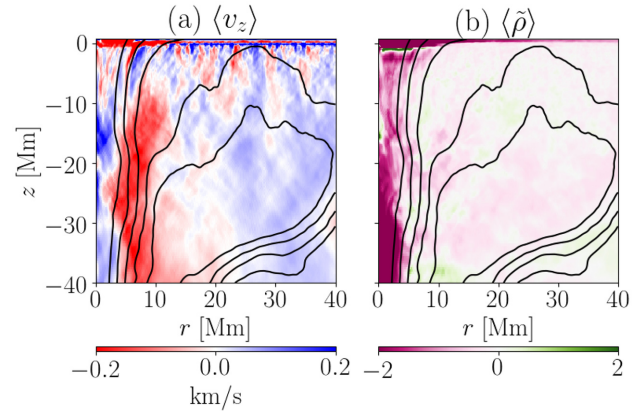


**Figure 15.** Azimuthally averaged values in the polar coordinate at  $t = 66$  h are shown. (Panel a) The vertical velocity ( $v_z$ ) and (panel b) normalized density ( $\tilde{\rho}$ ) are shown. The black contour lines show the magnetic flux evaluated from the centre of the coordinate ( $r = 0$ ). The values are from  $2 \times 10^{21}$  to  $1 \times 10^{22}$  Mx.

the same origin as the polar coordinate. Thus, we define the origin of the polar coordinate at every depth separately. We adopt the following procedure:

- (i) We estimate the magnetic flux of the positive vertical magnetic field in the left half of the computational domain ( $\Phi_+$ ).
- (ii) The threshold value of the magnetic flux ( $\Phi_s$ ) is 25 per cent of  $\Phi_+$ .
- (iii) We search the critical value  $B_c$  for the vertical magnetic field  $B_z$  with which the largest clump has a vertical magnetic flux of  $\Phi_s$ , where the definition of the clump is the continuous region in which the vertical magnetic field exceeds the critical value. The flux tube is identified with  $S_o$ .
- (iv) The origin of the polar coordinate ( $x_o, y_o$ ) at depth is defined with the following:

$$x_o = \frac{\int_{S_o} x B_z dS}{\int_{S_o} B_d dS}, \quad (24)$$

$$y_o = \frac{\int_{S_o} y B_z dS}{\int_{S_o} B_z dS}. \quad (25)$$

- (v) If  $\Phi_+$  is smaller than  $2.5 \times 10^{21}$  Mx, we use the origin of the polar coordinate defined at a place one grid below.

- (vi) The vertical profile of the origin of the polar coordinate is not smooth. We obtain the smooth profile of the origin of the polar coordinate with the Savitzky–Golay filter. The filtered profile is used for the origin of the polar coordinate in the following analyses.

Fig. 15 shows the azimuthally averaged profile of the vertical velocity (Fig. 15a) and the normalized density  $\tilde{\rho}$  (Fig. 15b) at  $t = 66$  h, where the parenthesis  $\langle \rangle$  shows the azimuthal average at constant radius  $r$ . The finding at a depth of 30 Mm is applicable to different depths. Except for the near-surface layer ( $z > -10$  Mm), the centre of the flux tube is filled with the upflow, surrounded by the coherent downflow in the outer side of the flux tube. The coherent upflow corresponds to low density (Fig. 15b), indicating that the driving mechanism of the upflow is the buoyancy.

### 3.6 Formation mechanism of sunspot

In this section, we discuss the formation mechanism of sunspots. The most important process for the formation of sunspots is

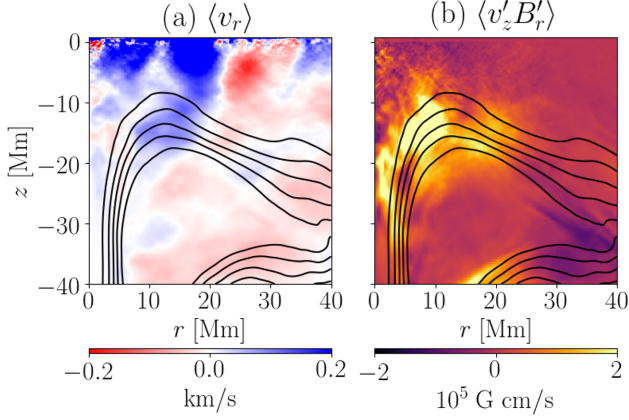


**Figure 16.** Azimuthally averaged values in the polar coordinate are shown. The values are averaged between  $t = 33$  and  $37$  h. (Panel a) The radial velocity  $\langle v_r \rangle$  and (panel b) one of the induction terms  $\langle v'_z B'_r \rangle$  are shown. The black contour lines are the same as in Fig. 15.

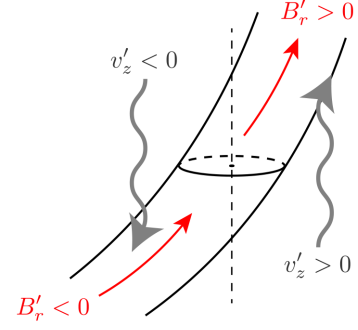
the collection of the magnetic flux toward the centre region. As discussed in Cheung et al. (2010), the temporal evolution of the magnetic flux is expressed as follows:

$$\begin{aligned} \frac{\partial \Phi_c}{\partial t} &= \frac{\partial}{\partial t} \int_S B_z dS \\ &= 2\pi r (\langle v_z \rangle \langle B_r \rangle - \langle v_r \rangle \langle B_z \rangle) \\ &\quad + 2\pi r (\langle v'_z B'_r \rangle - \langle v'_r B'_z \rangle), \end{aligned} \quad (26)$$

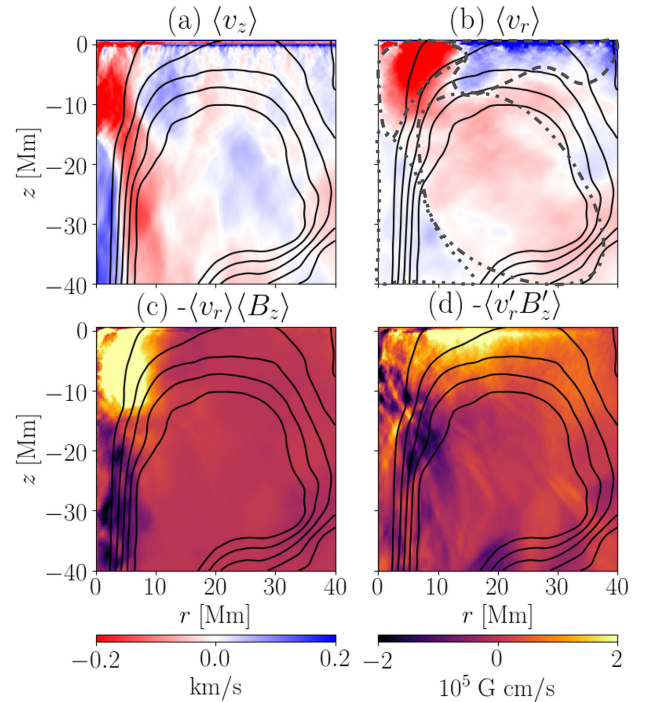
where area  $S$  is a circular area with fixed radius  $r$  at height  $z$ , and  $\langle \rangle$  shows the azimuthal average. Cheung et al. (2010) suggest that the essential term for collecting the magnetic flux at the photosphere is  $-\langle v'_r B'_z \rangle$ . This is caused by the mass loss at the highly inclined field (see fig. 8 in Cheung et al. 2010).

Fig. 16 shows the azimuthally averaged radial velocity ( $\langle v_r \rangle$ : panel a) and one of the turbulent induction terms ( $\langle v'_z B'_r \rangle$ : panel b). The definition of the origin of the polar coordinate is the same as that in Section 3.5. The values are averaged between  $t = 33$  and  $37$  h, and this range is around the emergence time, which is before the formation of the sunspot. At this time, the sunspot location in the near-surface is filled with the outflow from the centre to the outside, which is the negative effect for the generation of the sunspot. Among the induction terms, the most important contribution is from  $\langle v'_z B'_r \rangle$ . In Fig. 16(b); this term is positive in the magnetic flux. This can be explained with Fig. 17. The horizontal magnetic field with positive  $B_x$  can be regarded as a negative radial magnetic field ( $B'_r < 0$ ) in the downflow side ( $v'_z < 0$ ). In the upflow region ( $v'_z > 0$ ), the radial magnetic field is positive ( $B'_r > 0$ ). Both cause a positive correlation, meaning that before the formation of the sunspot, the shear of the downflow and the upflow are the most important mechanisms for the generation of the vertical magnetic flux.

Fig. 18 shows the azimuthally averaged flows and induction terms averaged between  $t = 47$  and  $53$  h, i.e. during the formation of sunspots. We find a strong coherent downflow and inflow at the near-surface layer ( $z > -15$  Mm) in the centre (Figs 18a and b, indicated with a dash-dotted line). This makes an important contribution to the collection of the vertical magnetic flux (Fig. 18c). This flow is transient and continues less than 10 h. While the existence of this downflow and inflow is not reported in Cheung et al. (2010), Rempel & Cheung (2014) show its



**Figure 17.** Schematic explaining the positive correlation of  $\langle v'_z B'_r \rangle$ . The red and black arrows show the direction of the magnetic field and flow, respectively. The dashed line shows the origin of the polar coordinate in this height.



**Figure 18.** Azimuthally averaged values in the polar coordinate during  $t = 47$  and  $53$  h are shown. (Panel a) The vertical velocity  $\langle v_z \rangle$ , (panel b) the radial velocity  $\langle v_r \rangle$ , (panel c) the induction terms  $-\langle v_r \rangle \langle B_z \rangle$ , and (panel d)  $-\langle v'_r B'_z \rangle$  are shown. The black contour lines are the same as in Fig. 15.

importance (see their fig. 11). The treatment of the bottom boundary would be important for the flow for calculations without the deep layer.

In the outer side of the sunspot, we see the Evershed-like outflow in the near-surface layer ( $-10$  Mm, indicated with a dashed line in Fig. 18b), which does not contribute to the loss of the vertical magnetic flux in this phase because the Evershed flow and the magnetic field line are roughly aligned (Fig. 18c). In the deeper layer, the sunspot core is filled with weak outflow, reducing the vertical magnetic flux in this phase (indicated with a dotted line in Fig. 18b). In the outer area, we also see weak inflow that does not play any role in the collection of the vertical flux (indicated with a dash-double-dotted line in Fig. 18b).

The most important contribution of the formation of the sunspot in the outer region is a turbulent induction term ( $-\langle v'_r B'_z \rangle$ ), which is

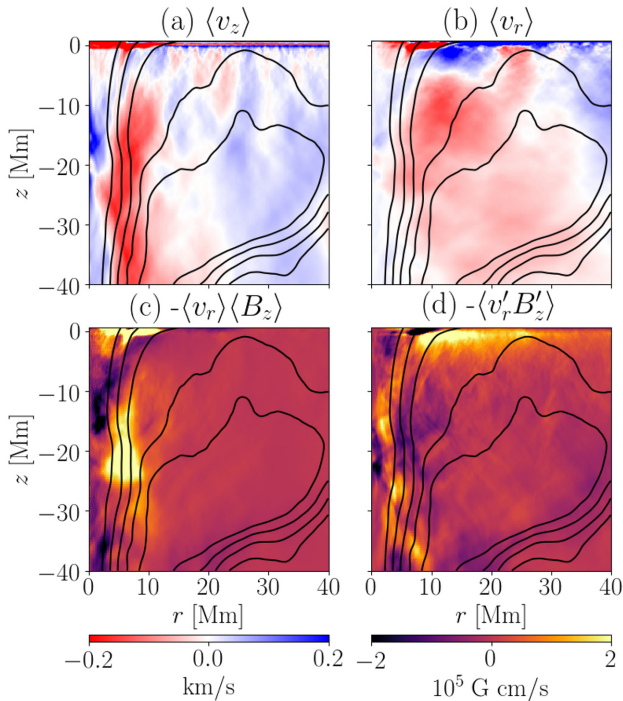


**Figure 19.** The format of the figure is the same as that in Fig. 18, but the values are averaged between  $t = 63$  and  $69$  h.

consistent with Cheung et al. (2010) and Rempel & Cheung (2014). The turbulent induction term ( $-\langle v_r' B_z' \rangle$ ) has a negative value in the deeper layer ( $z < -15$  Mm). Even the sum of all the induction terms has a negative value in the deep layer during the formation of the sunspot at the solar surface. Consequently, the decay of the sunspot starts during its formation.

### 3.7 Sunspot structure

In this section, we report the overall flow structure of the matured sunspot in comparison with the sunspot during formation.

Fig. 19 shows the azimuthally averaged flows and induction terms in the same manner as Fig. 18, but the values are averaged between  $t = 63$  and  $69$  h, in which the unsigned magnetic flux has its maximum value. Compared with the sunspot during formation, the strong coherent downflow and inflow in the near-surface layer disappear (Figs 19a and b), whereas weak downflow and inflow are seen in the near-surface layer ( $z > -5$  Mm). Nonetheless, the weak inflow still contribute to collecting the vertical magnetic flux in the near-surface layer (Fig. 19c). In the deep layer ( $z = -5$  to  $-20$  Mm), the root of the sunspot is filled with the outflow, which is connected to the Evershed-like flow in the outer area in the near-surface. This outflow in the middle layer makes an important contribution to the decay of the sunspot. In the deeper layer ( $z < -20$  Mm), the centre of the flux tube is filled with the upflow, as discussed in Section 3.5. This upflow is also connected to the outflow in the middle layer and the Evershed-like flow in the near-surface. We see coherent inflow in the outside the flux tube (Fig. 19b), which is connected to the downflow in the outer layer of the flux tube in the deeper layer. This coherent inflow makes a significant contribution to the collection of the magnetic flux, i.e. the maintenance of the sunspot. The turbulent induction term  $-\langle v_r' B_z' \rangle$  still makes a significant contribution to the maintenance of the sunspot in the near-surface layer, even if the sunspot is matured.

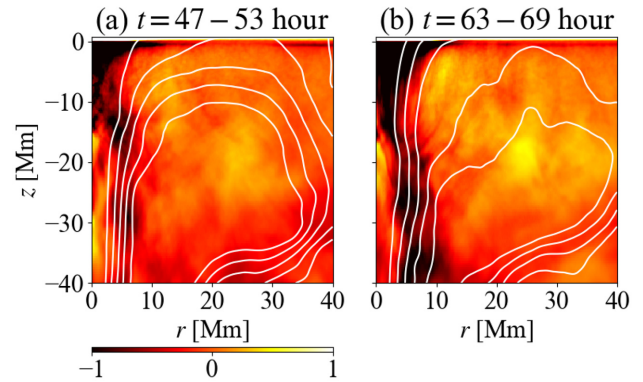


**Figure 20.** Azimuthally averaged normalized temperature  $\tilde{T}$  is shown. Panels (a) and (b) show the average value in  $t = 47$  and  $53$  h (during the sunspot formation) and  $t = 63$  and  $69$  h (matured sunspot), respectively.

Fig. 20 shows the azimuthally averaged normalized temperature  $\tilde{T}$  averaged between  $t = 47$  and  $53$  h (panel a, during the formation) and  $t = 63$  and  $69$  h (panel b, matured sunspot), where  $\tilde{T} = (T - \langle T \rangle_{\text{hd}}) / T_{\text{rms}(\text{hd})}$ . As the formation process of the sunspot proceeds, the low-temperature region expands because of the suppression of the convective energy transport and the radiative cooling at the photosphere. In both cases, we see a high-temperature region in the centre of the flux tube below a depth of  $-15$  Mm. While the phase of the sunspot formation is different in panels (a) and (b), the depth where the temperature changes from high to low does not change. In the matured sunspot, the coherent low-temperature region continues to a depth of  $40$  Mm.

## 4 SUMMARY AND DISCUSSION

In this study, we perform a numerical experiment of the flux emergence in an unprecedentedly deep domain that covers the whole convection zone from the base to the surface. The main purpose of this setting is to minimize the influence of the bottom boundary condition on the rising of the flux tube, formation of the sunspot, and internal structure of the generated sunspot.

The main findings of this study are summarized as follows:

- (i) The rising speed of the flux tube tends to be larger than the typical upward convection velocity because of the low density caused by the magnetic pressure and suppression of mixing.
- (ii) The rising speed of the flux tube exceeds  $250 \text{ m s}^{-1}$  at a depth of  $18$  Mm, while no clear evidence of the divergent flow 3 h before the emergence at the solar surface is seen.
- (iii) Initially, the root of the flux tube is filled with the downflows, and then the upflow fills the centre of the flux tube during the formation of the sunspot because of the low density.
- (iv) The essential mechanisms for the formation of the sunspot are the coherent inflow in the central region and the turbulent correlation  $-\langle v_r' B_z' \rangle$  in the outer region.
- (v) The low-temperature region is extended to a depth of at least of  $40$  Mm in the matured sunspot, with the high-temperature region in the centre of the flux tube.

Fig. 21 summarizes the flow and temperature structure of the sunspot during the formation (panel a) and matured phase (panel b). A large difference in the sunspot structure between the two phases is the strong coherent downflow/inflow to the centre of the sunspot down to a depth of  $15$  Mm during its formation. This downflow is significantly weakened in the matured sunspot and extends only

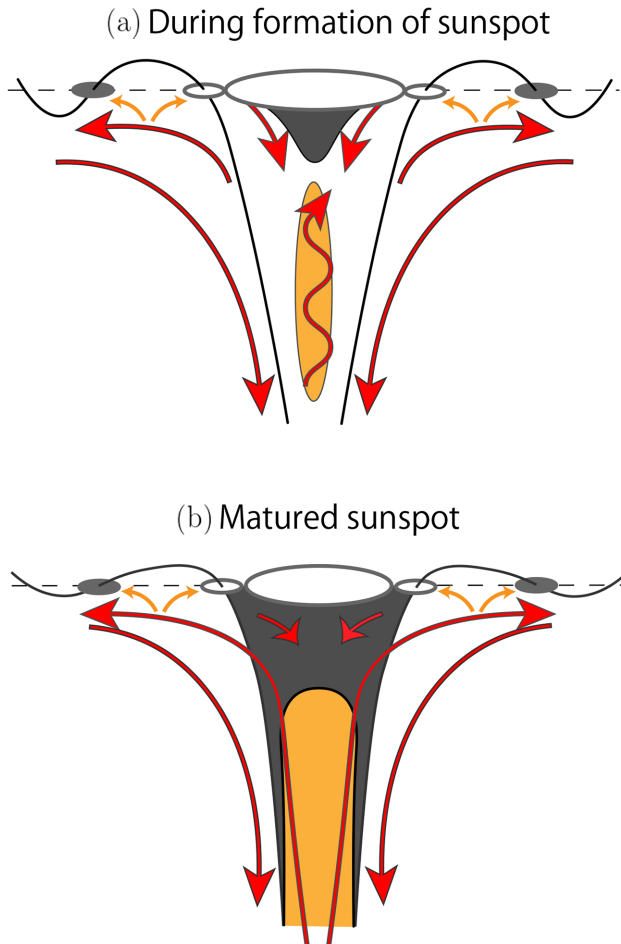


**Figure 21.** The summary of the sunspot structure during formation (panel a) and the matured sunspot (panel b). The red arrows show the coherent mean flow, and the orange arrows show the turbulent flow, which contributes to the collection of the magnetic flux. The black and orange areas correspond to low and high temperatures, respectively.

5 Mm further. The other difference between the two phases is the temperature structure. During the formation, the low-temperature region is mainly seen up to a depth of 10 Mm (some cooling is still seen at a depth of 30 Mm); a coherent low-temperature region is seen down to a depth of 40 Mm surrounding the high-temperature region in the centre of the flux tube.

#### 4.1 Reduced speed of sound technique

As discussed in Hotta et al. (2012), we need to keep the Mach number smaller than 0.7 in order to avoid the influence of the RSST. In this study, we keep the Mach number smaller than 0.1 when the RSST is used. Fig. 22 shows the RMS velocity in the hydrodynamic calculation without the magnetic field (panel a) and the Mach number estimated with the reduced speed of sound (panel b). The Mach number is always smaller than 0.1 at locations where the RSST is used (indicated with the dashed line in Fig 22b). Phenomena related with the magnetic field, i.e. the flux emergence and sunspot formation, occurs in a similar time scale as the thermal convection. For example, Fig. 13 shows that the up- and downflow are typically 200–300 m s<sup>-1</sup>, where the reduced speed of sound at  $z = -30$  Mm is about 4 km s<sup>-1</sup>. Thus, the Mach number is smaller

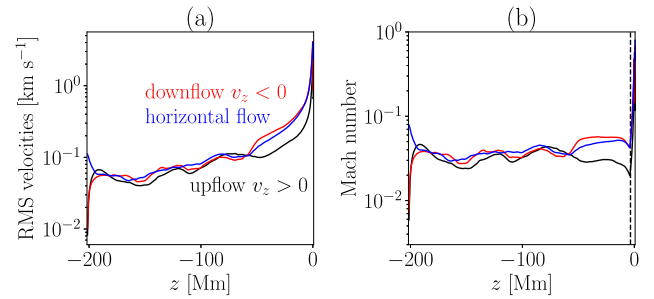


**Figure 22.** (Panel a) The rms velocity in the hydrodynamic calculation without the magnetic field and (panel b) the Mach number estimated with the reduced speed of sound are shown. The black, red, and blue lines show the results with upflow, the downflow, and the horizontal flow, respectively. Below the location indicated with the dashed line in panel (b), the RSST is used ( $\xi > 1$ ).

than 0.1 and we do not expect any significant influence of the RSST on the result shown in this paper.

#### 4.2 Computational domain

In this study, we prepare an unprecedentedly deep computational domain to minimize the bottom boundary influence. This also has a possible drawback on the convection structure. It is known that numerical simulations tend to overestimate the large-scale ( $> 30$  Mm) convection energy in the deep convection zone (Hanasoge, Duvall & Sreenivasan 2012; Lord et al. 2014). To reduce the power on a larger scale than the supergranulation, we intentionally prepare the small box in the horizontal direction of 100 Mm (see also Toriumi & Hotta 2019). This setting causes another side effect. Because of the insufficient horizontal box size and the periodic boundary condition, a generated sunspot is close to the sunspot on the other side. We expect that the calculation results in this study are not an evolution of the single isolated sunspot pair, but rather the sequence of the sunspot pairs. This fact mainly influences the decay of the sunspot, and we do not discuss this effect in detail in this study.

#### 4.3 Emergence rate

In this study, the emergence rate of the magnetic flux is  $9 \times 10^{20}$  Mx h<sup>-1</sup>, which is slightly larger than the 95 per cent confidence interval ( $7 \times 10^{20}$  Mx h<sup>-1</sup>, see Section 3.2) suggested by Namekata et al. (2019). There are several possible reasons for this discrepancy. The emergence rate would be determined by the rising speed and the structure of the magnetic flux tube. A fast-rising and intense structure of the flux tube tends to cause a high emergence rate. In this study, we find that the rising speed of the flux tube is not purely determined by the thermal convection; the magnetic effect is also important. Thus, there would be an appropriate initial setting of the magnetic flux tube for reproducing the emergence rate consistent with the observation. Parameter surveys for the initial setting of the flux tube should therefore be carried out in a future study.

In contrast, the number of observations is insufficient to conclude that our emergence rate is larger than reality. There are only several estimations of the emergence rate for the magnetic flux larger than  $10^{22}$  Mx (Toriumi, Hayashi & Yokoyama 2014). For example, Sun & Norton (2017) show  $1.12 \times 10^{21}$  Mx h<sup>-1</sup> for an instantaneous emergence rate. More observations are needed to identify the most probable flux tube structure in the deep convection zone.

## 4.4 Comparison with previous studies

### 4.4.1 Divergent flow prior to flux emergence

In this study, we find that the rising speed of the flux tube exceeds  $250 \text{ m s}^{-1}$  at a depth of 18 Mm, while we do not see any clear evidence of the divergent flow 3 h before the emergence time. This is inconsistent with Birch et al. (2016), who argue that the rising speed should not be larger than  $150 \text{ m s}^{-1}$  to have divergent flow at that time. This discrepancy can be caused by the settings in previous studies (Cheung et al. 2010; Rempel & Cheung 2014). In those studies, a magnetic flux tube has to be inserted kinematically from the bottom boundary because of the shallow calculation box. The speed of the rising flux tube is determined at the bottom boundary, and most of the flux tube has upward velocity. In this study, the flow structure of the flux tube is physically determined. The rising part of the flux tube has upflow, and its root initially has downflow. This natural determination of the rising speed would reduce the influence on the photosphere, i.e. the divergent flow. The constraints on the rising flux tube should be investigated in a deeper computational box, where the interaction of the convection and the magnetic field automatically determines the dynamics of the flux tube.

### 4.4.2 Upflow in flux tube

The other difference from previous studies is the upflow in the central region of the flux tube. Chen et al. (2017) found that the flux tube of the sunspot is filled with coherent downflow (see fig. 11 in their work). In their study, they use the data from the dynamo calculation (Fan & Fang 2014). They also find that the downflow region is the place for the sunspot because the converging flow to the downflow collects the magnetic flux. The flow structure does not change even after the sunspot is formed because the boundary condition is provided. In our study, we do not expect any boundary influence on the evolution of the flow in the flux tube, and the upflow in the central region with low density is a natural consequence of the MHD process.

Zhao & Kosovichev (2003) show the internal flow structure beneath the sunspot using the local helioseismology. They find converging motion with the downflow in the near-surface layer (depths of 0–3 Mm) and diverging motion with the upflow in the deeper layer (depths of 9–12 Mm). Our result for matured sunspots has a consistent flow structure (see Fig. 19). In addition, fig. 4 of Zhao & Kosovichev (2003) shows that the downflow and upflow are surrounded by the upflow and downflow, respectively, but this information is not explicitly mentioned in the paper. This feature is also consistent with our calculation.

## 4.5 Future perspective

Previously, flux emergence simulations in the deep convection zone with a thin-flux tube (D’Silva & Choudhuri 1993; Moreno-Insertis, Caligari & Schuessler 1995), anelastic approximation (Fan 2008; Weber et al. 2011), RSST (Hotta & Yokoyama 2012), and simulations around the solar surface (Cheung et al. 2010; Rempel & Cheung 2014; Chen et al. 2017) were almost completely separated. Our approach using the R2D2 code sheds light on connecting these two regions. This is an integral part of both the solar dynamo and the formation of the sunspot. Even in the simulation in this study with the computational domain of the whole convection zone, we still assume the initial magnetic flux tube condition because we have a very low vertical resolution in the deep convection zone ( $\sim 900 \text{ km}$ ).

To maintain the magnetic flux of the magnetic flux tube during the rising process from the base of the convection zone to the surface, we need to prepare a high resolution even in the deep convection zone (Cheung, Moreno-Insertis & Schüssler 2006). By using the current numerical resources, we are unable to achieve this purpose; however, we will soon be able to perform these types of calculations using next-generation supercomputers, such as Fugaku in Japan. In future studies, we plan to connect dynamo calculation and sunspot formation simulation in a calculation. This approach is expected to reveal the formation process of sunspots in a more self-consistent manner.

## ACKNOWLEDGEMENTS

The authors would like to thank the anonymous referee for the great suggestions. The authors are grateful to Kousuke Namekata for providing the detailed relation of the sunspot flux and the emergence rate. The results were obtained using the K computer at the RIKEN Advanced Institute for Computational Science (proposal Nos. hp190070, hp190183, hp180042, and ra000008). This work was supported by MEXT/JSPS KAKENHI grant Nos. JP19K14756, JP18H04436, JP16K17655, and JP15H05816. This research was supported by MEXT as Exploratory Challenge on Post-K Computer [Elucidation of the Birth of Exoplanets (Second Earth) and the Environmental Variations of Planets in the Solar System] and the Project for Solar-Terrestrial Environment Prediction.

## REFERENCES

- Auer L., 2003, in Hubeny I., Mihalas D., Werner K., eds, ASP Conf. Ser. Vol. 288, *Stellar Atmosphere Modeling*. Astron. Soc. Pac., San Francisco, p. 3
- Birch A. C., Schunker H., Braun D. C., Cameron R., Gizon L., Lipton B., Rempel M., 2016, *Sci. Adv.*, 2, e1600557
- Borrero J. M., Ichimoto K., 2011, *Living Rev. Sol. Phys.*, 8, 4
- Chen F., Rempel M., Fan Y., 2017, *ApJ*, 846, 149
- Cheung M. C. M., Moreno-Insertis F., Schüssler M., 2006, *A&A*, 451, 303
- Cheung M. C. M., Rempel M., Title A. M., Schüssler M., 2010, *ApJ*, 720, 233
- Christensen-Dalsgaard J. et al., 1996, *Science*, 272, 1286
- D’Silva S., Choudhuri A. R., 1993, *A&A*, 272, 621
- Fan Y., 2008, *ApJ*, 676, 680
- Fan Y., Fang F., 2014, *ApJ*, 789, 35
- Georgobiani D., Zhao J., Kosovichev A. G., Benson D., Stein R. F., Nordlund Å., 2007, *ApJ*, 657, 1157
- Ghizaru M., Charbonneau P., Smolarkiewicz P. K., 2010, *ApJ*, 715, L133
- Hanasoge S. M., Duvall T. L., Sreenivasan K. R., 2012, *Proc. Natl. Acad. Sci.*, 109, 11928
- Hathaway D. H., Choudhary D. P., 2008, *Sol. Phys.*, 250, 269
- Hotta H., Yokoyama T., 2012, *A&A*, 548, A74
- Hotta H., Rempel M., Yokoyama T., Iida Y., Fan Y., 2012, *A&A*, 539, A30
- Hotta H., Rempel M., Yokoyama T., 2015, *ApJ*, 798, 51
- Hotta H., Rempel M., Yokoyama T., 2016, *Science*, 351, 1427
- Hotta H., Iijima H., Kusano K., 2019, *Sci. Adv.*, 5, eaau2307
- Iijima H., Hotta H., Imada S., 2019, *A&A*, 622, A157
- Käpylä P. J., Mantere M. J., Brandenburg A., 2012, *ApJ*, 755, L22
- Leka K. D., Barnes G., Birch A. C., Gonzalez-Hernandez I., Dunn T., Javornik B., Braun D. C., 2013, *ApJ*, 762, 130
- Lord J. W., Cameron R. H., Rast M. P., Rempel M., Roudier T., 2014, *ApJ*, 793, 24
- Lundquist S., 1950, *Ark. Fys.*, 2, 361
- Moreno-Insertis F., Caligari P., Schuessler M., 1995, *ApJ*, 452, 894

- Namekata K. et al., 2019, *ApJ*, 871, 187  
 Nelson N. J., Brown B. P., Brun A. S., Miesch M. S., Toomre J., 2013, *ApJ*, 762, 73  
 Norton A. A., Jones E. H., Linton M. G., Leake J. E., 2017, *ApJ*, 842, 3  
 Otsuji K., Kitai R., Ichimoto K., Shibata K., 2011, *PASJ*, 63, 1047  
 Parker E. N., 1955, *ApJ*, 121, 491  
 Rempel M., 2012, *ApJ*, 750, 62  
 Rempel M., 2014, *ApJ*, 789, 132  
 Rempel M., Cheung M. C. M., 2014, *ApJ*, 785, 90  
 Rempel M., Schüssler M., Cameron R. H., Knölker M., 2009a, *Science*, 325, 171  
 Rempel M., Schüssler M., Knölker M., 2009b, *ApJ*, 691, 640  
 Rogers F. J., Swenson F. J., Iglesias C. A., 1996, *ApJ*, 456, 902  
 Stein R. F., Nordlund Å., 2012, *ApJ*, 753, L13  
 Sun X., Norton A. A., 2017, *Res. Notes Am. Astron. Soc.*, 1, 24  
 Toriumi S., Hotta H., 2019, *ApJ*, 886, L21  
 Toriumi S., Hayashi K., Yokoyama T., 2014, *ApJ*, 794, 19  
 Vögler A., Shelyag S., Schüssler M., Cattaneo F., Emonet T., Linde T., 2005, *A&A*, 429, 335  
 Wang Y. M., Sheeley N. R. J., 1991, *ApJ*, 375, 761  
 Weber M. A., Fan Y., Miesch M. S., 2011, *ApJ*, 741, 11  
 Zhao J., Kosovichev A. G., 2003, *ApJ*, 591, 446  
 Zwaan C., 1985, *Sol. Phys.*, 100, 397

## APPENDIX A: BACKGROUND STRATIFICATION

For the background stratification of  $\rho_0$ ,  $p_0$ ,  $T_0$ , and the other related variables, we use Model S (Christensen-Dalsgaard et al. 1996). Model S does not solve the entropy equation, and the entropy profile is not smooth. In contrast, in this study, the entropy equation is solved, and the tiny variation of the entropy is essential for the thermal convection property. To overcome this difficulty, we recalculate the hydrostatic equation with the help of the Model S. The hydrostatic equation is

$$\frac{dp_0}{dz} = -\rho_0 g. \quad (\text{A1})$$

We adopt the value of the gravitational acceleration  $g$  from the Model S, and we need to specify the distribution of the temperature or the entropy to relate the pressure  $p_0$  and the density  $\rho_0$ . We divide the solar convection zone into two parts at  $z = -3.5$  Mm. In the deep part, the entropy gradient is small, and we can regard it as adiabatic stratification. Thus, in this region, we adopt a constant value of the entropy at  $z = -3.5$  Mm in Model S.

In the upper part of the convection zone ( $z > -3.5$  Mm), the entropy gradient is significantly large. To obtain the smooth profile of the entropy gradient around the photosphere, we follow the following procedure:

- (i) Calculate the entropy gradient  $ds_0/dz$  using the entropy of the Model S.
- (ii) Use the Savitzky–Golay filter for the entropy gradient to obtain a smooth profile.
- (iii) Solve the hydrostatic equation using the filtered profile.

The black line in Fig. A1 shows the calculated entropy gradient in Model S. To reduce the jaggy feature in the entropy gradient, we use the Savitzky–Golay filter. The red line in Fig. A1 shows the filtered entropy gradient

In addition, the top boundary of Model S is about 500 km above the photosphere. We extend the stratification with the gravitational acceleration  $g(z) \propto \alpha(z + R_\odot)^{-2}$  and constant temperature, where we again note that  $z = 0$  corresponds to the surface of the sun.

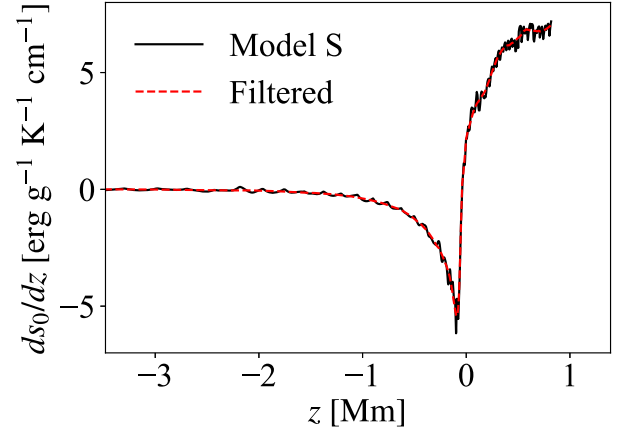


**Figure A1.** Entropy gradient in the upper part of the convection zone. The black line shows the original value in Model S, and the red line shows the filtered value.

## APPENDIX B: FOURTH-ORDER DERIVATIVE FOR INHOMOGENEOUS GRID

In this study, we adopt inhomogeneous grid spacing in the vertical direction  $z$ . To maintain the accuracy of the spatial derivative of the quantities, we adopt a general fourth-order formulation for inhomogeneous grid spacing as follows:

$$z_{i+2} - z_i = a, \quad (\text{B1})$$

$$z_{i+1} - z_i = b, \quad (\text{B2})$$

$$z_i - z_{i-1} = c, \quad (\text{B3})$$

$$z_i - z_{i-2} = d. \quad (\text{B4})$$

The first derivative of a quantity ( $q$ ) can be expressed as

$$\begin{aligned} \left(\frac{\partial q}{\partial z}\right)_i &= \frac{cd - b(c+d)}{(a-b)(a+c)(a+d)} q_{i+2} \\ &+ \frac{a(c+d) - cd}{(a-b)(b+c)(b+d)} q_{i+1} \\ &+ \frac{a(d-b) + bd}{(a+c)(b+c)(c-d)} q_{i-1} \\ &+ \frac{a(b-c) - bc}{(c-d)(a+d)(b+d)} q_{i-2}. \end{aligned} \quad (\text{B5})$$

## APPENDIX C: RADIATION TRANSFER

To evaluate the heat and the cooling of the radiation ( $Q$  in equation (4)), we solve the radiation transfer equation

$$\frac{\partial I}{\partial \tau} = -I + S, \quad (\text{C1})$$

where  $I$  is the radiative intensity,  $S = \sigma T^4/\pi$  is the source function, and  $\sigma$  is the Stefan–Boltzman constant. In this study, we use the Rosseland mean opacity for the grey radiation transfer. Every quantity in the MHD equations is defined in the cell centre, and the value at the cell surface is needed for the radiation transfer. To this end, we adopt the linear interpolation for the logarithmic value:

$$q_{i+1/2} = \exp \left[ \frac{\ln(q_i) + \ln(q_{i+1})}{2} \right]. \quad (\text{C2})$$

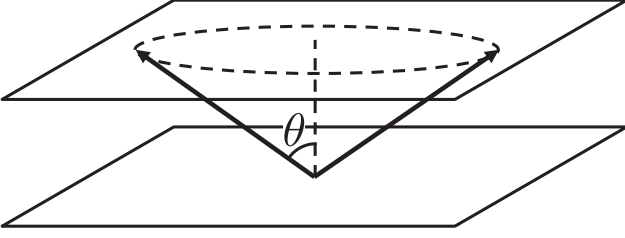


**Figure C1.** Schematic of our treatment of the radiative transfer. The arrow shows a ray inclined from the vertical axis with the angle of  $\theta$ . We assume the azimuthal homogeneity of the radiative intensity and that the radiative energy is transported only upward and downward.

In this study, we treat only vertically upward and downward radiation energy transport. We solve rays inclined to the vertical axis (Fig. C1). The inclination is expressed as  $\mu = \cos \theta$  with  $\mu = 1/\sqrt{3}$ . Then, the intensity is azimuthally averaged for evaluating the radiative heating ( $Q$ ). For example, we explain the upward radiation transfer from  $z_{i-1/2}$  to  $z_{i+1/2}$ , where  $z_{i+1/2} = (z_{i+1} + z_i)/2$ . As a first step, we evaluate the optical depth between  $z_{i-1/2}$  and  $z_{i+1/2}$  along a ray, which is expressed as

$$\Delta\tau = \frac{1}{\mu} \int_{z_{i-1/2}}^{z_{i+1/2}} \rho\kappa dz, \quad (\text{C3})$$

where  $\kappa$  is the opacity. We assume that the logarithmic value of  $\alpha = \rho\kappa$  is a linear function in the space  $z$ :

$$\ln \alpha(z) = \ln \alpha_{i-1/2} + \frac{\ln \alpha_{i+1/2} - \ln \alpha_{i-1/2}}{z_{i+1/2} - z_{i-1/2}} (z - z_{i-1/2}). \quad (\text{C4})$$

Then, equation (C3) can be integrated analytically, and the solution is

$$\Delta\tau = \frac{1}{\mu} \frac{(\alpha_{i+1/2} - \alpha_{i-1/2}) (z_{i+1/2} - z_{i-1/2})}{\ln \alpha_{i+1/2} - \ln \alpha_{i-1/2}}. \quad (\text{C5})$$

Equation (C5) includes a singularity at  $\alpha_{i-1/2} = \alpha_{i+1/2}$ . To avoid the singularity, we use a different expression for  $\Delta\tau$  using the Taylor expansion around  $\alpha_{i-1/2} = \alpha_{i+1/2}$  as

$$\Delta\tau = \frac{1}{\mu} \left[ \frac{\alpha_{i-1/2}^2}{3\alpha_{i+1/2} - \alpha_{i-1/2}} + \frac{\alpha_{i+1/2}^2}{3\alpha_{i+1/2} - \alpha_{i-1/2}} \right] (z_{i+1/2} - z_{i-1/2}). \quad (\text{C6})$$

When the upward radiation transfer is considered, the intensity at the cell surface ( $I_{i+1/2}$ ) is determined by the intensity in the downstream

cell surface ( $I_{i-1/2}$ ) with the formal solution of the radiation transfer equation:

$$I_{i+1/2} = I_{i-1/2} \exp(-\Delta\tau) + \int_0^{\Delta\tau} S(\Delta\tau') \exp(-\Delta\tau + \Delta\tau') d(\Delta\tau'). \quad (\text{C7})$$

To solve equation (C7) analytically, we follow a similar procedure for the evaluation of the optical depth. While the linear function (Vögler et al. 2005) and the second-order Bézier curve (Auer 2003) are used for the source function in previous studies, we adopt the linear function for the logarithmic values:

$$\ln S(\Delta\tau') = \ln S_{i-1/2} + \frac{\ln S_{i+1/2} - \ln S_{i-1/2}}{\Delta\tau} \Delta\tau'. \quad (\text{C8})$$

Then, equation (C7) is solved analytically as

$$I_{i+1/2} = I_{i-1/2} \exp(-\Delta\tau) + \Delta\tau \frac{S_{i+1/2} - S_{i-1/2} \exp(-\Delta\tau)}{\ln S_{i+1/2} - \ln S_{i-1/2} + \Delta\tau}. \quad (\text{C9})$$

The downward radiation can be calculated using the same method in the opposite direction.

When the upward and downward intensities on the cell surface ( $I_{(\text{up})i+1/2}$ , and  $I_{(\text{dw})i+1/2}$ , respectively) are evaluated, the radiative heating is calculated in two ways depending on the optical depth. For the small optical depth  $\tau$ , we use the expression

$$Q_{(\text{J})i} = 4\pi\rho_i\kappa_i (J_i - S_i), \quad (\text{C10})$$

$$J_i = \frac{I_{(\text{up})i+1/2} + I_{(\text{up})i-1/2} + I_{(\text{dw})i+1/2} + I_{(\text{dw})i-1/2}}{4}. \quad (\text{C11})$$

For the large optical depth:

$$Q_{(\text{F})i} = -\frac{F_{(\text{rad})i+1/2} - F_{(\text{rad})i-1/2}}{\Delta z}, \quad (\text{C12})$$

$$F_{(\text{rad})i+1/2} = 2\pi\mu (I_{(\text{up})i+1/2} - I_{(\text{dw})i+1/2}). \quad (\text{C13})$$

We switch these expressions around  $\tau = 0.1$  as follows:

$$Q_i = Q_{(\text{J})i} \exp\left(-\frac{\tau}{\tau_0}\right) + Q_{(\text{F})i} \left[1 - \exp\left(-\frac{\tau}{\tau_0}\right)\right], \quad (\text{C14})$$

where  $\tau_0=0.1$ . The validation of this method is detailed in our previous publication (Hotta et al. 2019).

This paper has been typeset from a  $\text{\LaTeX}$  file prepared by the author.